

## Analysis and control of high sideslip manoeuvres

Christoph Voser , Rami Y. Hindiyeh & J. Christian Gerdes

To cite this article: Christoph Voser , Rami Y. Hindiyeh & J. Christian Gerdes (2010) Analysis and control of high sideslip manoeuvres, Vehicle System Dynamics, 48:S1, 317-336, DOI: [10.1080/00423111003746140](https://doi.org/10.1080/00423111003746140)

To link to this article: <https://doi.org/10.1080/00423111003746140>



Published online: 26 Nov 2010.



Submit your article to this journal [↗](#)



Article views: 708



View related articles [↗](#)



Citing articles: 9 View citing articles [↗](#)

## Analysis and control of high sideslip manoeuvres

Christoph Voser<sup>a</sup>, Rami Y. Hindiyeh<sup>b\*</sup> and J. Christian Gerdes<sup>b</sup>

<sup>a</sup>Department of Mechanical and Process Engineering, ETH Zurich, Raemistrasse 101, 8092 Zurich, Switzerland; <sup>b</sup>Department of Mechanical Engineering, Stanford University, Terman Engineering Center Rm. 536, 380 Panama Mall, Stanford, CA 94305-4021, USA

(Received 19 October 2009; final version received 1 March 2010)

This paper presents simple analytical techniques that are used to understand and control high sideslip drift manoeuvres of road vehicles. These are manoeuvres in which a skilled driver stabilises a vehicle beyond its limits of handling, an operating regime responsible for major safety concerns in everyday driving. An analysis of the equilibria of a bicycle model with nonlinear tyres reveals the existence of unstable ‘drift equilibria’ corresponding to cornering at high sideslip angle in a countersteer configuration. Equipped with this information, linearisation about a desired drift equilibrium is used to design a controller that stabilises the vehicle at the equilibrium. The controller is subsequently implemented on a steer- and drive-by-wire testbed and successfully used to achieve autonomous drifts.

**Keywords:** high sideslip manoeuvres; drifting; steering control; vehicle control; nonlinear vehicle dynamics

### 1. Introduction

#### 1.1. Background

High sideslip manoeuvres, commonly known as drifting, are a dramatic and unique cornering technique in which a vehicle is stabilised beyond its limits of handling at a large sideslip angle  $\beta$ .  $\beta$ , as defined in Equation (1), is given by the arctangent of the ratio of the vehicle’s lateral velocity  $v_y$  at the centre of gravity (CG) to its longitudinal velocity  $v_x$  at the CG:

$$\beta = \arctan \frac{v_y}{v_x}. \quad (1)$$

Geometrically, this represents the angle between the longitudinal axis of the vehicle and the direction of the vehicle’s velocity vector at the CG. Therefore, a high sideslip manoeuvre roughly corresponds to the vehicle cornering while it is travelling ‘sideways’ to some extent.

Manoeuvres of this nature are fairly common in competitive driving on loose, low friction surfaces, such as rally and dirt track racing. Skilled drivers in these types of racing execute

---

\*Corresponding author. Email: hindiyeh@stanford.edu

drifts by abruptly inducing rear tyre saturation using brakes or throttle, thereby destabilising the vehicle. They then stabilise the vehicle as it begins to spin by holding it in a high sideslip configuration through a combination of steering opposite the direction of the turn ('counter-steer') and throttle inputs. Thus, drifting corresponds to an unusual control technique in which a vehicle is stabilised beyond its limits of handling.

Needless to say, this bears little resemblance to the activities of the average driver. When cornering, the average driver operates the vehicle at low sideslip, well within the limits of handling, with the tyre lateral forces below their friction limits. In contrast, drifting inherently requires operation of the vehicle beyond the limits of handling. Generally, the average driver only enters this operating regime when the vehicle has been inadvertently destabilised, which is of course dangerous for both the driver and any surrounding traffic. Therefore, an in-depth analysis of drifting and high sideslip manoeuvres provides valuable insights into nonlinear vehicle dynamics and control in an operating regime that is responsible for major safety concerns in everyday driving.

## 1.2. Previous work

The dynamics of drifting and drift control techniques in particular have not been thoroughly explored in the previous research. Nonetheless, literature contains several examples of research that has shed some light upon the purpose, characteristics, and control of drifting.

Several works have applied optimisation-based techniques to produce drift-like behaviour in simulation under conditions often present in dirt track and rally racing. Gustaffsson [1] applied optimal control techniques to calculate the optimal lap time for racing circuits of various configurations. Under certain circumstances, such as hairpin turns that are common in rally circuits, the optimisation yielded techniques that are mainly used in rally car driving, including high sideslip pendulum turns. Along similar lines, Velenis and Tsiotras [2] examined the problem of maximising exit velocity at the conclusion of a 90° turn, and found optimal trajectories that are drift-like in nature on low friction surfaces. In both cases, however, the high sideslip behaviour was transient (in contrast to a sustained drift) and produced through an explicit sequence of control inputs calculated by the optimisation routine, as opposed to a more general, analytically derived control law. Furthermore, these analyses were only performed in a simulation environment and not validated with experimental measurements.

Other researchers, such as Abdulrahim [3] and Edelmann *et al.* [4], have drawn interesting conclusions through analysis of experimental measurements of high sideslip manoeuvres performed by skilled drivers. Both these authors concluded that drivers executing these manoeuvres utilise a combination of countersteer and throttle inputs in order to stabilise the vehicle in a drift. Furthermore, a stability analysis conducted in Edelmann *et al.* [4] verified that the steady-state cornering conditions corresponding to drifting are inherently unstable, and control inputs from the driver are in fact required in order to achieve a sustained drift.

This work elaborates upon these analyses in order to achieve a more complete understanding of the dynamics and stability of drifting. In particular, a major contribution of this work is an understanding of drifting from a control development perspective, with a simpler model than in previous works that facilitates the design of an experimentally validated controller for autonomous drifting. Phase portrait and bifurcation analysis techniques inspired by the work of Ono *et al.* [5] and Liaw *et al.* [6] are used on a bicycle model with nonlinear tyres to determine vehicle equilibria corresponding to drifting along with their stability and controllability characteristics. This information is used to design simple steering and longitudinal controllers based upon linearisation of the bicycle model about a desired drift equilibrium. Finally, the controllers are implemented on a steer- and drive-by-wire testbed and shown to hold the vehicle in a sustained drift successfully.

## 2. Vehicle and tyre models

This work utilises the two-state model shown in Figure 1. In this model, the front and rear tyres are lumped into a single tyre at each axle and the vehicle's motion is planar, so pitch and roll motions are neglected. Longitudinal dynamics are also neglected and the vehicle's longitudinal velocity  $v_x$  is treated as a time-varying system parameter. The vehicle states are its lateral velocity  $v_y$  at the CG in body-fixed coordinates and yaw rate  $r$  (rotation rate normal to the plane). The input to the model is the front tyre steer angle  $\delta$ . The governing equations for the system in terms of these states are given in Equations (2) and (3):

$$\dot{v}_y = \frac{F_{y,f} \cos \delta + F_{y,r}}{m} - r v_x = f_1(v_y, r, \delta), \quad (2)$$

$$\dot{r} = \frac{a F_{y,f} \cos \delta - b F_{y,r}}{I_z} = f_2(v_y, r, \delta), \quad (3)$$

where  $m$  is the vehicle mass,  $I_z$  the vehicle's yaw inertia,  $a$  the distance from the vehicle CG to the front axle,  $b$  the distance from the vehicle CG to the rear axle,  $F_{y,f}$  the front tyre lateral force, and  $F_{y,r}$  the rear tyre lateral force.

The tyre lateral forces  $F_{y,f}$  and  $F_{y,r}$  are calculated using a variant of the Fiala lateral tyre force model [7], as given in Equation (4):

$$F_y(\alpha) = \begin{cases} -C_\alpha \tan \alpha + \frac{C_\alpha^2(2 - \mu_s/\mu_p)}{3\mu_p F_z} |\tan \alpha| \tan \alpha \\ -\frac{C_\alpha^3(1 - 2\mu_s/3\mu_p)}{9\mu_p^2 F_z^2} \tan^3 \alpha, & |\alpha| < \alpha_{sl}, \\ -\mu_s F_z \operatorname{sgn} \alpha, & |\alpha| \geq \alpha_{sl}, \end{cases} \quad (4)$$

$$\alpha_{sl} = \arctan \frac{3\mu_p F_z}{C_\alpha},$$

where  $C_\alpha$  is the tyre cornering stiffness,  $F_z$  the normal load applied to the tyre,  $\mu_p$  the peak friction coefficient between the tyre and the ground,  $\mu_s$  the sliding coefficient of friction between the tyre and the ground, and  $\alpha$  the tyre slip angle. The slip angles  $\alpha_f$  and  $\alpha_r$  of the front and rear lumped tyres of the bicycle model are calculated in terms of  $v_y$ ,  $r$ , and  $v_x$  as follows in Equations (5) and (6):

$$\alpha_f = \arctan \frac{v_y + ar}{v_x} - \delta = \alpha_{f,0} - \delta, \quad (5)$$

$$\alpha_r = \arctan \frac{v_y - br}{v_x}. \quad (6)$$

This vehicle model does not explicitly account for vehicle behaviours that are significant at and beyond the limits of handling, in particular the effect of longitudinal tyre force and

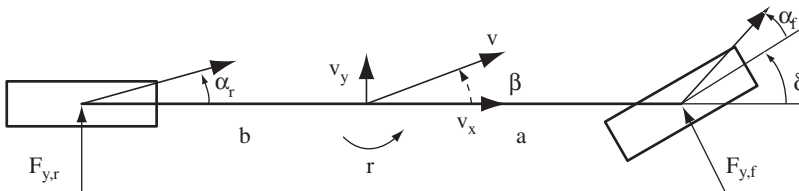


Figure 1. The bicycle model.

lateral–longitudinal tyre force coupling. Nonetheless, it is possible to account for the overall effect of these behaviours through tyre model parameters, as discussed below.

### 3. Parameter identification

In order to conduct system analysis and control design with the model outlined in Section 2, it is necessary to identify the parameters in this model for the vehicle testbed and testing surface used in this work. Weight, inertia, and weight distribution are known from direct measurement, while tyre parameters are estimated from experimental data obtained on the testing surface. All simulations and analysis presented in the remainder of this work have been produced using a bicycle model with the parameter set given in this section.

#### 3.1. Testbed and testing surface

The experimental results for this work have been generated using P1, an all-electric by-wire research platform built entirely by students at Stanford University [8]. This vehicle, shown in Figure 2, features steer- and drive-by-wire capability, an extensive sensor suite, online state estimation, rear wheel drive, and regenerative braking. Relevant weight, inertia, and weight distribution parameters are listed in Table 1.

P1's sensor suite includes an Inertial Navigation System (INS) with automotive-grade accelerometers and gyroscopes for all six degrees of freedom, a single antenna Global Positioning System (GPS) receiver for position and velocity measurements, and a two antenna GPS receiver for heading and roll angle measurements. State estimates are produced via GPS/INS sensor fusion using Kalman filters for roll, heading, and velocity states [9]. Previous work has shown that the state estimates produced using this technique and sensor suite are sufficient for vehicle control purposes [10].

All the experimental data presented in this work have been obtained at a large parking lot near Stanford University, consisting of asphalt covered by a thin layer of gravel. The low



Figure 2. P1, the by-wire testbed.

Table 1. P1 parameters.

Distance CG to front axle	$a$	1.35	(m)
Distance CG to rear axle	$b$	1.15	(m)
Vehicle mass	$m$	1724	(kg)
Yaw inertia	$I_z$	1300	(kg m <sup>2</sup> )

friction characteristics of this surface facilitate experimental work at and beyond the limits of handling at lower, relatively safe speeds.

### 3.2. Tyre model identification

The usage of the Fiala tyre model in Equation (4) necessitates identification of the cornering stiffness and friction coefficients for each tyre. This is accomplished through fits of empirical tyre curves and time-domain experimental data, as detailed below.

#### 3.2.1. Empirical tyre curves

Empirical tyre curves are generated from data of a quasi-steady state ramp steer manoeuvre. In this manoeuvre, the front steer angle is slowly ( $0.5 \text{ deg s}^{-1}$ ) increased so that the vehicle can be assumed to be in a steady state condition ( $\dot{r} = \dot{v}_y = 0$ ). Under this assumption, the lateral acceleration  $a_y$  can be approximated as in Equation (7). Figure 3 indicates close agreement between a measurement of  $a_y$  for the ramp steer manoeuvre and the associated steady state approximation, validating the above assumption:

$$a_y^{ss} = r v_x. \quad (7)$$

Applying the steady state approximation to the bicycle model in Equations (2) and (3) leads to the expressions below for the front and rear tyre lateral forces:

$$F_{y,f} = \frac{mb}{(a+b)\cos\delta} v_x r = \frac{mb}{(a+b)\cos\delta} a_y^{ss}, \quad (8)$$

$$F_{y,r} = \frac{ma}{a+b} v_x r = \frac{ma}{a+b} a_y^{ss}. \quad (9)$$

By using Equations (8) and (9) to calculate the tyre lateral forces and the relations in Equations (5) and (6) to calculate the tyre slip angles, it is possible to generate experimental tyre curves like the ones given by the scatter plots in Figure 4(a) and (b). These curves reflect the

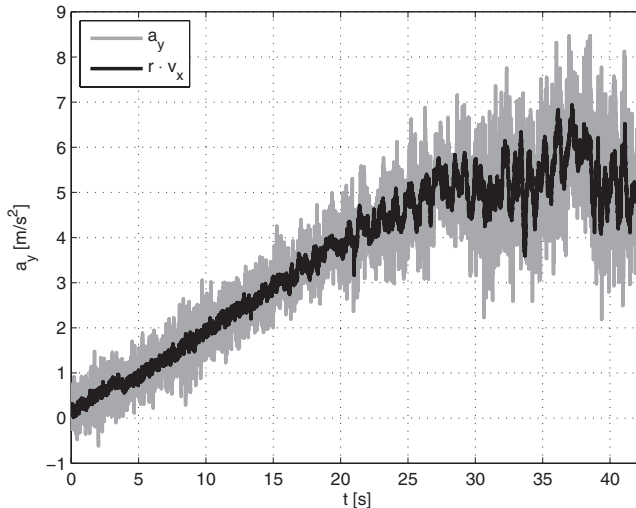


Figure 3. Comparison of measured lateral acceleration and its steady state approximation.

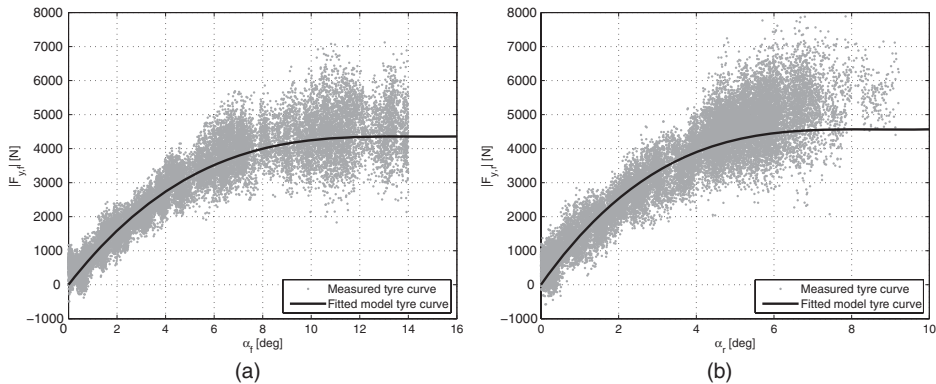


Figure 4. Empirical tyre curve and model fit: (a) front and (b) rear.

limit understeer characteristic of the car, in which the front tyre curve exhibits saturation while the rear tyre curve does not. Furthermore, no peak is evident in either tyre curve, indicating that it is possible to simplify the tyre model for this test surface by assuming that  $\mu_s = \mu_p$  for both tyres. As a consequence, it is only necessary to determine single coefficients of friction  $\mu_f$  and  $\mu_r$  for the front and rear tyres, respectively.

### 3.2.2. Front tyre model identification

The front empirical tyre curve contains data up to, and well beyond, the point of tyre force saturation. As a consequence, it is possible to identify a cornering stiffness  $C_{\alpha,f}$  and friction coefficient  $\mu_f$  for the front tyre by simply fitting the Fiala model to the front empirical tyre curve. This identification is sufficient for the purposes of this work because the front wheels of the P1 testbed are not driven; as a consequence, the front empirical tyre curve represents pure lateral force data that is valid up to and beyond the handling limits. The black line in Figure 4(a) shows the Fiala model fit to the front empirical tyre curve. This fit yields the values for  $C_{\alpha,f}$  and  $\mu_f$  Table 2.

### 3.2.3. Rear tyre model identification

The cornering stiffness  $C_{\alpha,r}$  of the rear tyre can be obtained using a linear fit to the rear empirical tyre curve (Figure 4b) at small slip angles. The rear friction coefficient  $\mu_r$ , however, cannot be obtained from the empirical tyre curve. Aside from the obvious lack of data in the saturation region, this is because the empirical tyre curve was obtained under conditions approximating pure cornering. Under such conditions, a relatively small amount of longitudinal force is applied at the rear tyre, whereas the high sideslip manoeuvres under consideration in this work involve significant longitudinal forces at the rear tyre. Consequently, what is desired is an ‘effective’ rear friction coefficient that reflects an average rear tyre lateral force capacity in the presence of significant applied longitudinal force and lateral-longitudinal force coupling.

Table 2. Tyre parameter estimates.

Front cornering stiffness	$C_{\alpha,f}$	57,500	(N/rad)
Rear cornering stiffness	$C_{\alpha,r}$	92,500	(N/rad)
Front friction coefficient	$\mu_f$	0.56	[–]
Rear friction coefficient	$\mu_r$	0.5	[–]

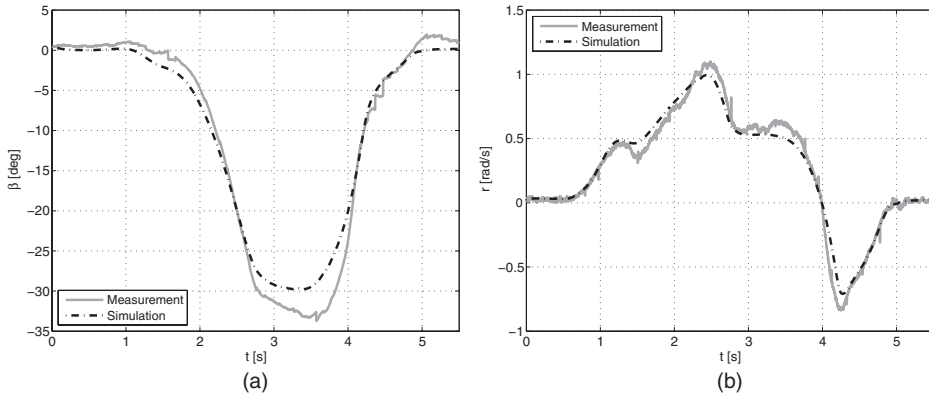


Figure 5. Comparison of measurements and simulation for manual high sideslip manoeuvre: (a)  $\beta$  and (b)  $r$ .

As a result,  $\mu_r$  is obtained by matching simulation predictions of yaw rate and sideslip with measurements of these quantities during a high sideslip manoeuvre. The time-domain fits are accomplished by taking the steering input and longitudinal velocity measurements from a high sideslip data set and using them as inputs to a bicycle model simulation with all tyre parameters except  $\mu_r$  fixed. The yaw rate and sideslip predictions of the simulation are compared with the experimental measurements of these quantities, and the  $\mu_r$  value within the simulation is varied until close agreement is achieved. Figure 5(a) and (b) compares simulation predictions (black) with experimental data of a manoeuvre (grey), in which a driver destabilised the vehicle and then briefly held the vehicle at high sideslip. The simulation predictions, in particular for yaw rate, are good and capture the overall qualitative characteristics of the manoeuvre. The  $\mu_r$  which is used to achieve this fit is given in Table 2. The black line plotted in Figure 4(b) gives the Fiala tyre curve resulting from the cornering stiffness and friction coefficient identified for the rear tyre.

It is important to note from Table 2 that  $\mu_r < \mu_f$ , which is consistent with the influence of significant applied longitudinal force at the rear tyre. Lateral–longitudinal force coupling via the friction circle dictates that the lateral force generating capability of a tyre is reduced as more longitudinal force is applied at the tyre. This reduction in capability can be represented by a reduction in the effective friction coefficient of the tyre.

## 4. Nonlinear system analysis

### 4.1. Equilibrium analysis

Edelmann *et al.* [4] established that sustained drifting is a steady state cornering condition, albeit an unstable one. From a modelling standpoint, steady state cornering conditions correspond to equilibria of the bicycle model dynamics ( $\dot{r} = \dot{\beta}_y = 0$ ). Thus, the differential equations given in Equations (2) and (3) are reduced to the system of algebraic equations in Equation (10):

$$\begin{aligned} \frac{F_{y,f}^{\text{eq}} \cos \delta^{\text{eq}} + F_{y,r}^{\text{eq}}}{m} - r^{\text{eq}} v_x &= f_1(v_y^{\text{eq}}, r^{\text{eq}}, \delta^{\text{eq}}) = 0, \\ \frac{a F_{y,f}^{\text{eq}} \cos \delta^{\text{eq}} - b F_{y,r}^{\text{eq}}}{I_z} &= f_2(v_y^{\text{eq}}, r^{\text{eq}}, \delta^{\text{eq}}) = 0. \end{aligned} \quad (10)$$



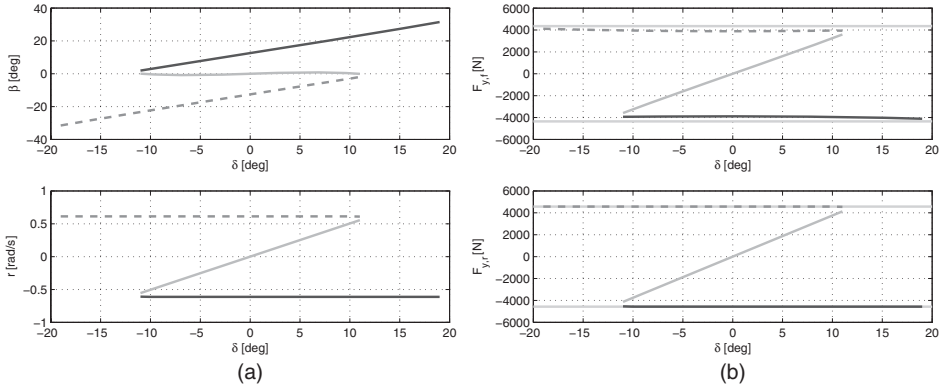


Figure 6. (a) Equilibrium states for  $v_x = 8 \text{ ms}^{-1}$  and (b) equilibrium tyre lateral forces for  $v_x = 8 \text{ ms}^{-1}$ .

For a specified constant  $v_x$  and constant  $\delta^{\text{eq}}$ , Equation (10) becomes a system of two equations in the two unknowns  $v_y^{\text{eq}}$  and  $r^{\text{eq}}$  that can be solved numerically to determine steady state cornering conditions. By repeating this process for a wide range of  $\delta^{\text{eq}}$ , it is possible to generate diagrams like those given in Figure 6(a) and (b). Figure 6(a) shows the equilibrium sideslip angle and yaw rate as a function of the steer angle  $\delta^{\text{eq}}$  for  $v_x = 8 \text{ ms}^{-1}$ . Figure 6(b) gives the corresponding equilibrium front and rear tyre forces as a function of  $\delta^{\text{eq}}$  as compared with the friction limits for each tyre, indicated by horizontal, light grey lines.

From these diagrams, it is evident that the bicycle model exhibits two distinct classes of equilibria. The family of equilibria shown with a grey solid line corresponds to cornering within the limits of handling. This is evidenced by the fact that neither the front nor the rear tyre equilibrium lateral forces are saturated at these equilibria, and by the comparatively small  $\beta^{\text{eq}}$  for these equilibria. In contrast, the families of equilibria shown with dashed dark grey and solid black lines correspond to steady state cornering at comparatively large  $\beta^{\text{eq}}$ . At these equilibria,  $F_{y,r}^{\text{eq}}$  is saturated and  $F_{y,f}^{\text{eq}}$  is large but unsaturated. For larger magnitude  $\delta^{\text{eq}}$ ,  $\delta^{\text{eq}}$  and  $r^{\text{eq}}$  for these two groups of equilibria have opposite sign, meaning that the vehicle is in a countersteer configuration. The countersteer, high sideslip, and rear tyre saturation characteristics of the dark grey and black equilibria suggest that they correspond to the left and right-handed drifts, respectively. Interestingly, there appears to be a linear relationship between  $\delta^{\text{eq}}$  and  $\beta^{\text{eq}}$  for each set of drift equilibria.

Consistent with the findings of Ono *et al.* [5], the number of system equilibria varies with  $\delta^{\text{eq}}$  as a result of a bifurcation in the system dynamics. For  $\delta^{\text{eq}} \in [-11, 11]$  deg, the model has an unsaturated equilibrium, a left-handed drift equilibrium, and a right-handed drift equilibrium. For  $\delta^{\text{eq}} < -11^\circ$  and  $\delta^{\text{eq}} > 11^\circ$ , the model only has a single drift equilibrium. With their large countersteer angles and very large sideslip angles, it is these solitary equilibria that correspond to drifting in its most recognisable form.

#### 4.2. Sensitivity analysis of drift equilibria

In rally and dirt track racing, drifts are executed on surfaces whose friction properties change constantly. Furthermore, the longitudinal velocity for these manoeuvres will also vary, as skilled drivers do not necessarily want to maintain a fixed speed during a manoeuvre. This motivates an analysis of the sensitivity of the drift equilibria to friction and longitudinal

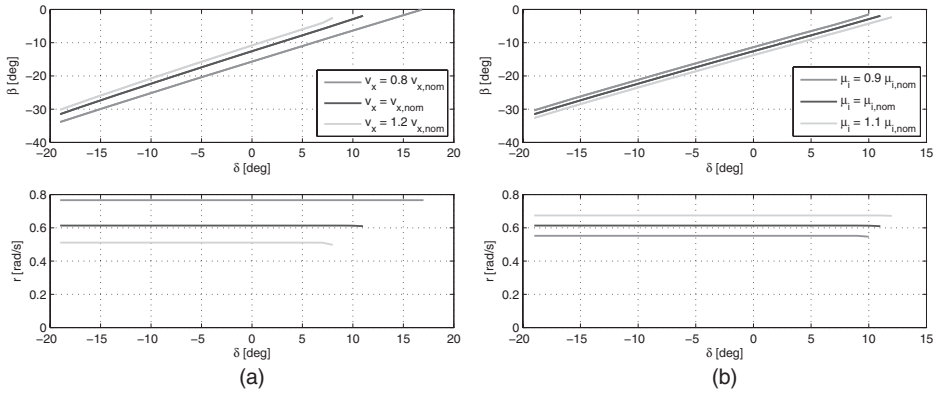


Figure 7. Drift equilibrium states for changing (a)  $v_x$  and (b) friction.

velocity changes. Since the drift equilibria are symmetric, only left-hand drifts are considered below.

Figure 7(a) shows the variation in equilibrium sideslip and yaw rate for a  $\pm 20\%$  variation in speed. Figure 7(b) shows the variation in the equilibrium states for a  $\pm 10\%$  variation in friction at both the front and rear tyres (the ratio between the coefficients remains the same). In either case, the equilibrium yaw rate exhibits somewhat significant variation. This is not surprising, however, given that the steady state yaw rate is linearly related to steady state acceleration (and therefore friction) and inversely related to longitudinal velocity (Equation (7)).

In contrast, equilibrium sideslip angle shows remarkably little sensitivity to variations in longitudinal velocity or friction. A  $\pm 20\%$  variation in longitudinal velocity leads to variations of sideslip angle of no more than  $2.5^\circ$ , while a  $\pm 10\%$  variation in friction leads to variations on the order of only  $1.2^\circ$ . In both cases, the linear relationship between  $\beta^{\text{eq}}$  and  $\delta^{\text{eq}}$  highlighted in Section 4.1 is preserved, with little or no variation in slope.

The insensitivity of equilibrium sideslip angle to both longitudinal velocity and friction variation provides some rationale for the prevalence of high sideslip cornering in racing on surfaces where friction is uncertain. Both the small variation in  $\beta^{\text{eq}}$  and the robust linear relationship between  $\delta^{\text{eq}}$  and  $\beta^{\text{eq}}$  suggest that steady cornering by drifting possesses some constant, predictable handling characteristics as friction and longitudinal velocity vary. Consequently, high sideslip cornering techniques that are forgiving of changing surface conditions may provide a safer, more reliable means to negotiate a turn than conventional cornering techniques, which require more exacting knowledge of surface conditions.

#### 4.3. Phase portrait and bifurcation analysis

While the equilibrium analysis of Section 4.1 sheds light upon the different types of equilibria of the bicycle model and the existence of a bifurcation, it does not provide insight into the stability characteristics of the equilibria or the type of bifurcation. With this in mind, a phase portrait analysis and an eigenvalue analysis of the system's linearisation are used to answer these questions.

Phase portraits provide a visualisation of the system equilibria and dynamics in the system's state space. They are generated in this particular case by simulating the bicycle model's response at a fixed  $\delta$  and  $v_x$  for a multitude of initial conditions and plotting all of the resulting state trajectories in the  $(\beta, r)$  plane. For all the phase portraits presented below,  $v_x = 8 \text{ ms}^{-1}$ .

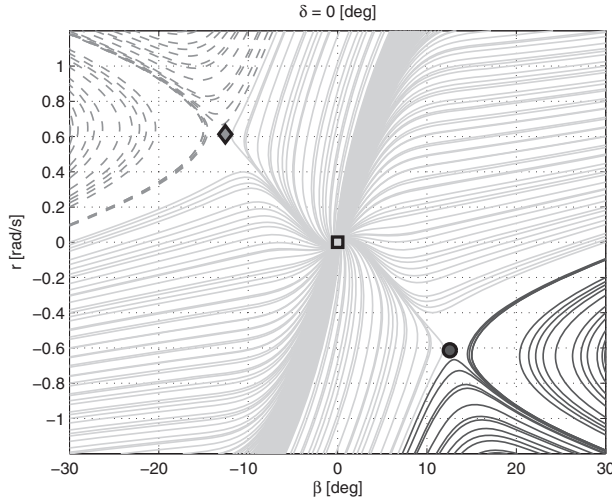


Figure 8. Phase portrait for  $\delta = 0^\circ$ .

#### 4.3.1. Stability analysis ( $\delta = 0^\circ$ )

Since the bicycle model has an unsaturated equilibrium and two drift equilibria when  $\delta = 0^\circ$ , the phase portrait for this steer angle is ideal for a graphical analysis of the stability characteristics of the two types of equilibria. Figure 8 gives the phase portrait for  $\delta = 0^\circ$ .

The local stability characteristics of the three equilibria are readily identified from Figure 8:

- (1) The unsaturated equilibrium (square) is located at the origin ( $\beta = 0, r = 0$ ) and is a stable node. This is evident from the fact that state trajectories in the neighbourhood of the equilibrium are attracted to the equilibrium. Furthermore, a linearisation of the system about the equilibrium has negative, real, distinct eigenvalues. This result makes intuitive sense, as the condition represented by the unsaturated equilibrium is simply straight ahead driving of a nominally stable vehicle.
- (2) The equilibrium point in the second quadrant (diamond) is a left-handed drift equilibrium. It is graphically evident that this equilibrium is an unstable saddle point, as no state trajectories converge at this point. This is confirmed by the linearisation of the system about the equilibrium, which has one real, negative eigenvalue and one real, positive eigenvalue. This is consistent with the results of Edelmann *et al.* [4], in that the saddle point equilibrium corresponds to the steady state, unstable cornering conditions associated with drifting in Edelmann *et al.* [4].
- (3) The third and final equilibrium is located in the fourth quadrant (circle). It has the same properties as the equilibrium in the second quadrant, but corresponds to a right-hand drift equilibrium.

Three different state subspaces can be identified surrounding the three equilibria:

- (1) Stabilisable turn subspace (light grey trajectories): state trajectories that begin in this region converge to the origin. This subspace represents the set of initial conditions for which the vehicle will end up travelling straight ahead.
- (2) Unstable left-hand turn subspace (dashed dark grey trajectories): state trajectories in this region do not converge to the stable cornering conditions. For example, a vehicle that initially has a yaw rate of  $0.4 \text{ rad s}^{-1}$  and a sideslip angle of  $-25^\circ$  has a saturated rear tyre.

The moment imbalance about the vehicle's  $z$ -axis makes the yaw rate grow. Initially, the sideslip angle dynamics are dominated by the tyre forces  $F_{y,f} \cos \delta + F_{y,r}$ , which leads to a decrease of  $|\beta|$ . Eventually, however, the yaw rate increases to the point that it becomes the dominant term in the sideslip angle dynamics. As a result,  $|\beta|$  also grows. The fact that  $|\beta|$  initially decreases in this thought experiment before increasing suggests that the  $\beta$  dynamics are non-minimum phase in the vicinity of the drift equilibria. Surely enough, the transfer function from steer angle perturbations  $\Delta\delta$  to sideslip angle perturbations  $\Delta\beta$  around the drift equilibrium has a right half plane zero that corroborates this insight, as shown in Equation (11):

$$\frac{\Delta\beta(s)}{\Delta\delta(s)} = \frac{7.24(s - 14.32)}{(s - 2.4)(s + 5.61)}. \quad (11)$$

- (3) Unstable right-hand turn subspace (solid dark grey trajectories): This region possesses the same overall characteristics as the unstable left-hand turn subspace.

#### 4.3.2. Bifurcation characteristics

As the roadwheels are progressively turned further to the right, the positioning of the equilibria in the phase portrait shifts until a bifurcation finally occurs. For  $\delta = -5^\circ$  (Figure 9), the stable unsaturated equilibrium moves away from the origin into the third quadrant, where it corresponds to stable right-hand cornering. At the same time, the saddle point corresponding to a right-hand drift equilibrium moves closer to the  $y$ -axis, while the left-hand drift equilibrium moves away from the  $y$ -axis.

This trend continues as the steer angle becomes more negative, until the unsaturated equilibrium and right-hand drift equilibrium finally 'collide' in the fourth quadrant. At this point, the equilibria annihilate each other, resulting in what is known as a saddle-node bifurcation. The end effect of this bifurcation is evident from the phase portrait for  $\delta = -15^\circ$  (Figure 10), in which the left-hand drift saddle point is the sole equilibrium of the system. Since this equilibrium is unstable, no state trajectories converge to the equilibrium and there is no stabilisable turn subspace in open-loop.

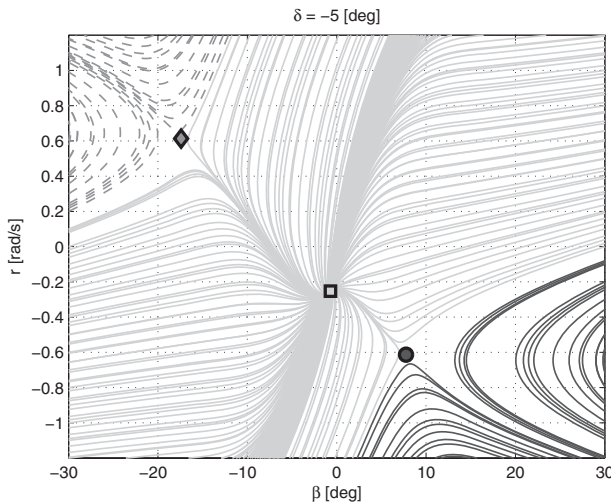


Figure 9. Phase portrait for  $\delta = -5^\circ$ .

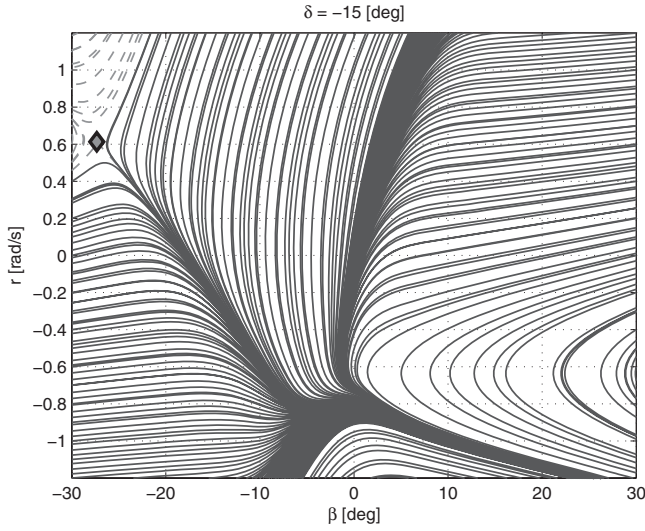


Figure 10. Phase portrait for  $\delta = -15^\circ$ .

## 5. Controller design

### 5.1. Analysis of drift by human driver

Analysis of a high sideslip manoeuvre executed by a human driver provides some insight into a control strategy for reproducing such manoeuvres via autonomous control on P1. In particular, the data given in Figure 11(a) and (b) suggest that autonomous drift manoeuvres can be partitioned into open-loop and closed-loop segments.

During the initial portion of the manoeuvre ( $t = 0$  s to  $t \approx 0.75$  s), the vehicle is made to corner near the limits of handling. The driver accomplishes this by ramping to a roughly constant steer angle of  $\sim 15^\circ$ . From  $t \approx 0.75$  s to  $t \approx 1.5$  s, regenerative braking is applied at the rear wheels using P1's electric motors. As a consequence, rear tyre saturation occurs due to coupling of lateral and longitudinal tyre forces via the friction circle. Furthermore,

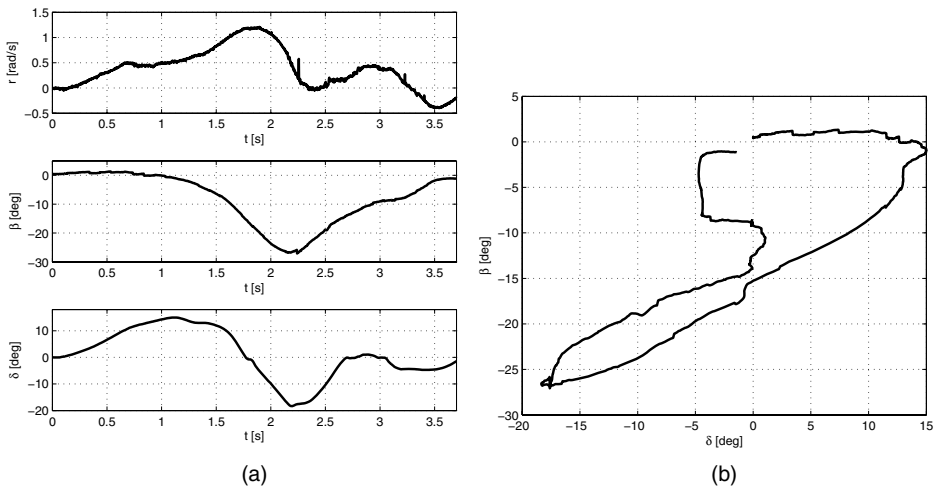


Figure 11. Measurements of user-executed drift.

deceleration induces weight transfer to the front axle of the vehicle, reducing the total force capacity of the rear tyre. The net effect of these phenomena is a sudden reduction in the rear tyre lateral force, leading to a sudden increase in the yaw moment.

This increase in yaw moment causes the peaking in yaw rate evident in Figure 11(a) from  $t \approx 1$  s to  $t \approx 1.75$  s. Due to the  $-rv_x$  term in the lateral velocity dynamics shown in Equation (2), this yaw rate build-up leads to an increase in lateral velocity magnitude, and therefore an increase in sideslip magnitude as well. Thus, the regenerative braking acts as a mechanism by which to destabilise the vehicle and initiate a transition to a larger sideslip magnitude.

During this initiation process, the driver does not make significant changes to the steering input. This is apparent from Figure 11(b), in which the steer angle does not change considerably as the sideslip magnitude begins to grow. However, as soon as the sideslip angle falls below  $-5^\circ$ , the  $(\beta, \delta)$  relationship assumes an entirely different characteristic, in which a strong correlation exists between the sideslip and steer angles. As the sideslip grows in magnitude, so does the extent of countersteer in order to prevent a vehicle spinout. Conversely, as the sideslip magnitude decreases, countersteer decreases in an effort to avoid an exit from the drift (the driver is unsuccessful in preventing the exit in this instance). It is this correlation between sideslip and steer angle that indicates that the driver is actively attempting to control the high sideslip manoeuvre using steering after the sideslip angle magnitude has become sufficiently large.

These observations motivate a two-stage approach for executing an autonomous drift in which an open-loop sequence is used to produce initial conditions appropriate for activation of a closed-loop controller. In particular, the open-loop sequence consists of cornering near the limits of handling and destabilisation of the vehicle via regenerative braking. The resulting sideslip build-up guides the vehicle's state trajectory into the vicinity of the desired drift equilibrium, at which point closed-loop control is activated. This strategy guides the development of controllers for autonomous drifting that are designed to be activated when the state trajectory closely approaches the desired drift equilibrium.

## 5.2. Longitudinal controller

The analyses presented in Section 4 assume a constant longitudinal velocity. With this in mind, the longitudinal controller used in this work consists of a simple proportional speed controller designed to maintain the vehicle longitudinal velocity  $v_x$  near some desired value  $v_x^{\text{des}}$  corresponding to the constant longitudinal velocity used in the analyses. The control law, given in Equation (12), feeds back the longitudinal velocity error  $\Delta v_x = v_x - v_x^{\text{des}}$  to compute a voltage command  $U_{\text{mot}}$  to P1's drive-by-wire system:

$$U_{\text{mot}} = K_{v_x} \Delta v_x. \quad (12)$$

## 5.3. Steering controller

The steering control law is designed based upon the linearisation of the bicycle model about the desired drift equilibrium  $(v_y^{\text{eq}}, r^{\text{eq}})$ . As such, it consists of a constant term given by the equilibrium steer angle  $\delta^{\text{eq}}$  for the desired drift equilibrium plus a steering addition  $\Delta\delta$  computed by feeding back the errors  $\Delta v_y = v_y - v_y^{\text{eq}}$  and  $\Delta r = r - r^{\text{eq}}$  in the lateral velocity and yaw rate, respectively:

$$\delta = \delta^{\text{eq}} + \Delta\delta = \delta^{\text{eq}} - K_{v_y} \Delta v_y - K_r \Delta r. \quad (13)$$

The lateral velocity error  $\Delta v_y$  is fed back rather than the sideslip angle error  $\Delta\beta$  because  $\Delta\beta$  feedback would introduce a coupling between the longitudinal and steering controllers that would complicate analysis and design.

The state feedback gains  $K_{vy}$  and  $K_r$  are designed using the state-space form of the linearisation of the system. This form is given by Equation (14), where  $\mathbf{x} = [\Delta v_y, \Delta r]^T$ ,  $\mathbf{u} = \Delta \delta$ , and the system matrices  $\mathbf{A}$  and  $\mathbf{B}$  are calculated according to Equation (15).

$$\dot{\mathbf{x}} = \mathbf{A}\mathbf{x} + \mathbf{B}\mathbf{u}, \quad (14)$$

$$\mathbf{A} = \begin{bmatrix} \frac{\partial}{\partial v_y} f_1(v_y, r, \delta) & \frac{\partial}{\partial r} f_1(v_y, r, \delta) \\ \frac{\partial}{\partial v_y} f_2(v_y, r, \delta) & \frac{\partial}{\partial r} f_2(v_y, r, \delta) \end{bmatrix}_{v_y^{\text{eq}}, r^{\text{eq}}, \delta^{\text{eq}}}, \quad \mathbf{B} = \begin{bmatrix} \frac{\partial}{\partial \delta} f_1(v_y, r, \delta) \\ \frac{\partial}{\partial \delta} f_2(v_y, r, \delta) \end{bmatrix}_{v_y^{\text{eq}}, r^{\text{eq}}, \delta^{\text{eq}}}. \quad (15)$$

Defining a gain matrix  $\mathbf{K} = [K_{vy}, K_r]$ , closed-loop stability of the system is achieved when the eigenvalues of  $\mathbf{A} - \mathbf{BK}$  have negative real part. From this condition, the stable gain subspace is defined by Equation (16), where  $A_{ij}$  and  $B_i$  are elements of the  $\mathbf{A}$  and  $\mathbf{B}$  matrices, respectively. The maximum lateral velocity gain is only system dependent, whereas the minimum yaw rate gain is linearly dependent on  $K_{vy}$ :

$$K_{vy} < K_{vy, \text{crit}} = \frac{\det(\mathbf{A})B_2 - (B_2A_{11} - A_{21}B_1)\text{trace}(\mathbf{A})}{B_1B_2\text{trace}(\mathbf{A}) - A_{12}B_2^2 - A_{21}B_1^2}, \quad (16)$$

$$K_r > K_{r, \text{crit}} = \frac{\text{trace}(\mathbf{A}) - B_1K_{vy}}{B_2}.$$

The gain space that yields closed-loop stability is divided into two subspaces: one which contains real-valued poles [light grey points in Figure 12(a)] and another with complex and therefore oscillatory poles (dark grey). The subspaces are separated by a ‘ridge’ [black line in Figure 12(a) and (b)]. For a given  $K_r$ , the lateral velocity gain which results in real and maximally negative poles lies on this ‘ridge’.

#### 5.4. Activation of steering controller

As discussed in Section 5.1, the autonomous drift manoeuvre to be performed by the research vehicle has been partitioned into open-loop and closed-loop segments, with the open-loop segment designed to create initial conditions suitable for activation of the closed-loop steering

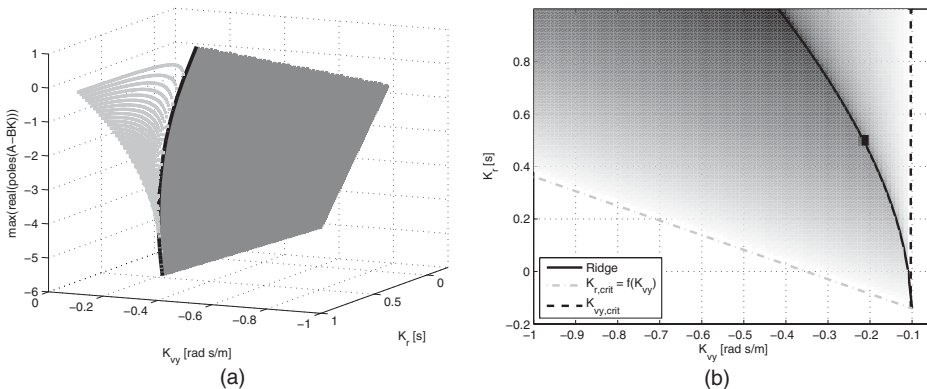


Figure 12. (a) Maximum real part of  $\text{eig}(\mathbf{A} - \mathbf{BK})$  for various gain combinations. Light grey: real poles, dark grey: complex poles, black: ‘ridge’. (b) The  $(K_{vy}, K_r)$  gain space: darker shades denote smaller maximum real part of  $\text{eig}(\mathbf{A} - \mathbf{BK})$ .



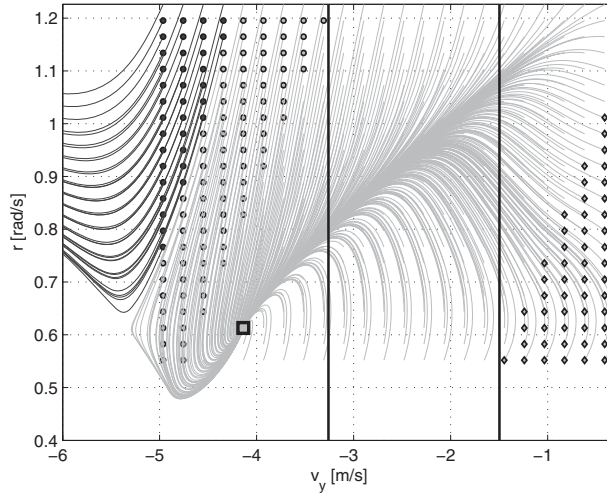


Figure 13. Phase portrait of the vehicle with closed-loop control.

controller for drifting. A phase portrait analysis of the closed-loop dynamics of the system about the drift equilibrium informs the selection of these initial conditions. In Figure 13, state trajectories of the closed-loop system are plotted for a multitude of initial conditions surrounding the desired drift equilibrium. The state trajectories have been generated using a bicycle model of P1 accounting for the steering limits of the vehicle ( $-21^\circ \leq \delta \leq 21^\circ$ ). The controller gains lie on the ‘ridge’ in the  $(K_{vy}, K_r)$  gain space as described in Section 5.3.

Consistent with the selection of controller gains to achieve negative, real-valued eigenvalues, the desired equilibrium is a stable node. However, this equilibrium is not globally stable, as indicated by the divergent trajectories shown in black. On such trajectories, the steer angle input is saturated at full countersteer ( $\delta = -21^\circ$ ), which is insufficient to prevent the vehicle from spinning out along these trajectories.

Nonetheless, there is a considerable portion of the state space in which trajectories do stabilise to the desired equilibrium. These trajectories are shown in light grey in Figure 13. The shape of these state trajectories provides some interesting insights into the mechanism by which the controller stabilises the vehicle to the desired equilibrium. In particular, it appears that the initial response of the controller is to generate a significant change in yaw rate accompanied by minimal change in lateral velocity, after which both states monotonically converge to the desired equilibrium value.

It is also interesting to note that the stability of trajectories is dictated largely by initial lateral velocity. For a given initial lateral velocity, stable trajectories exist across a wide range of initial yaw rates. This suggests that a simple lateral velocity threshold for activation of the steering controller is sufficient to place the vehicle on a state trajectory that converges to the desired drift equilibrium in the phase portrait.

However, this threshold must be selected carefully in order to avoid trajectories on the boundaries of the stable region for which actuator limitations become apparent. Initial conditions leading to such trajectories have been marked in Figure 13 with diamonds or circles. These two categories of trajectories are described below:

- **Diamonds:** Initial conditions in this region correspond to activation of the controller at comparatively low magnitudes of yaw rate and lateral velocity. In response, the steering controller attempts to steer significantly into the turn, reaching the left steering limit



( $\delta = 21^\circ$ ) and saturating the front tyre lateral force as a consequence. Because of the ‘de-rated’  $\mu_r$  within this model, state trajectories that begin at low magnitude lateral velocity still converge to the desired drift equilibrium. In reality, the high sideslip conditions under which the ‘de-rated’  $\mu_r$  was obtained are not reflected at these initial conditions, and front tyre lateral force saturation will prevent the vehicle’s state trajectory from entering the stabilising region of the state space.

- Circles: At these initial conditions, the vehicle’s lateral velocity is well beyond the desired equilibrium value, and the vehicle is in danger of spinning out. As a consequence, the controller countersteers to the right steering limit ( $\delta = -21^\circ$ ). Although this is sufficient to stabilise the vehicle for these trajectories, a slight increase in initial lateral velocity will result in a spin due to the steering limit and front tyre saturation.

In light of these observations, it makes sense to activate the steering controller based upon a lateral velocity threshold  $v_y^{\text{thres}}$  within the two black vertical lines shown in Figure 13. For this range of thresholds, controller activation is insensitive to the initial yaw rate at controller activation and actuator limitations are avoided.

## 6. Experimental investigation

The controllers described in the preceding section have been implemented on the P1 testbed described in Section 3.1. This section describes the details of the implementation and discusses the results obtained using this control method.

### 6.1. Controller parameters

The drift equilibrium corresponding to  $\delta^{\text{eq}} = -15^\circ$ , discussed in Section 4.3, is chosen as the desired equilibrium in the experimental implementation of the controller. Table 3 summarises the characteristics of this equilibrium and the controller parameters used to stabilise the equilibrium.

As in Section 5.4, the feedback gains have been selected so that the poles of the closed-loop system lie on the ‘ridge’ in the gain space described in Section 5.3. The gain selection is not particularly aggressive in order to avoid saturation of the testbed’s steering system. The black square in Figure 12 indicates the location of the steering controller gains in the  $(K_{vy}, K_r)$  gain space.

An experimentally determined open-loop steering and longitudinal control sequence based upon the observations of Section 5.1 is used to destabilise the vehicle. Once the lateral velocity passes a threshold  $v_y^{\text{thres}}$  within the range established in Figure 13, the steering controller is activated. For simplicity, the longitudinal controller is activated when the longitudinal velocity falls below an experimentally determined threshold  $v_x^{\text{thres}}$ .

Table 3. Equilibrium and controller details.

Equilibrium point			Controller parameters		
$\delta^{\text{eq}}$	−15	(deg)	$K_{vx}$	−1	(Vs/m)
$v_x^{\text{eq}}$	8	(m s <sup>−1</sup> )	$K_{vy}$	−0.22	(rad/m)
$v_y^{\text{eq}}$	−4.13	(m s <sup>−1</sup> )	$K_r$	0.5	(rad)
$r^{\text{eq}}$	0.613	(rad s <sup>−1</sup> )	$v_y^{\text{thres}}$	−2.8	(m s <sup>−1</sup> )
			$v_x^{\text{thres}}$	8.8	(m s <sup>−1</sup> )

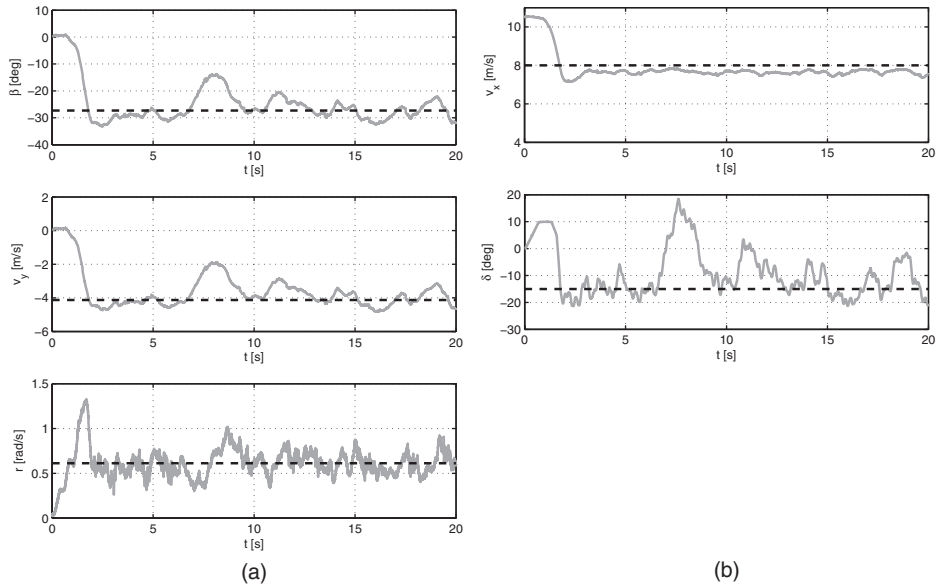


Figure 14. Measurements of autonomous drift: (a)  $\beta$ ,  $v_y$ , and  $r$ , (b)  $v_x$ , and  $\delta$ .

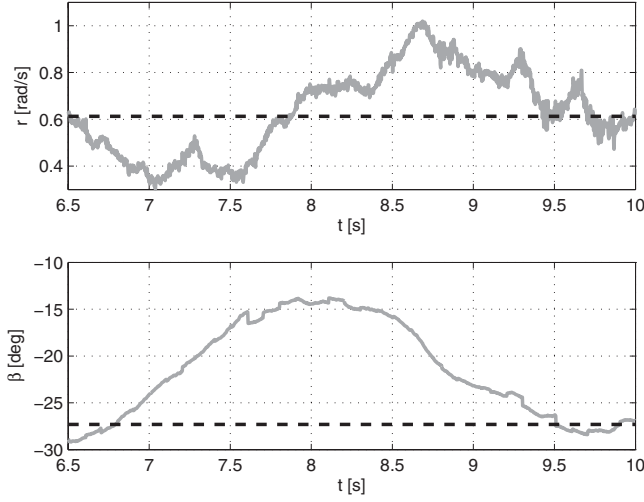
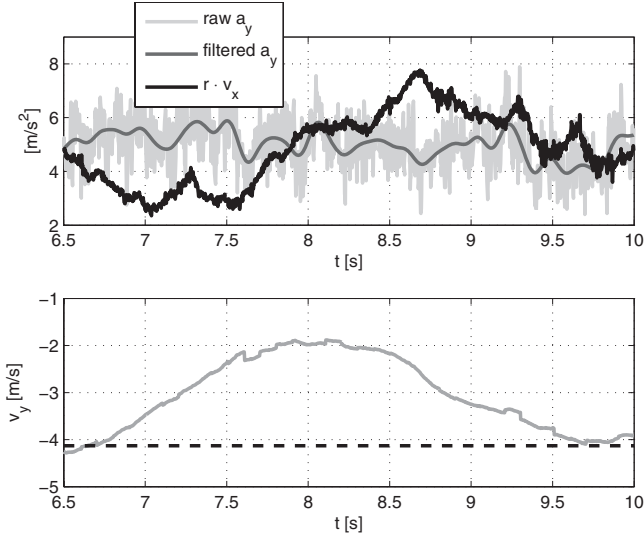
## 6.2. Successfully sustained high sideslip angle manoeuvre

Figure 14(a) and (b) shows the measurements of an autonomous left-hand drift manoeuvre as achieved using the initiation sequence and controller parameters described above. From the plot of sideslip in Figure 14(a), it is clear that the vehicle successfully enters a sustained drift at a high sideslip angle, with the sideslip angle and yaw rate varying about their desired equilibrium values (indicated by dashed lines). These results validate the use of the bicycle model and tyre parameter identification techniques described in this work for the purpose of identifying drift equilibria and designing control to stabilise these equilibria.

At  $t = 6.5$  s, a disturbance acts upon the system, as indicated by an abrupt drop in yaw rate and large deviation of lateral velocity from its desired value. This disturbance is likely the result of an increase in friction on the testing surface that causes the testbed to nearly exit from the drift. Fortunately, the steering controller breaks out of countersteer and steers into the turn to bring the sideslip and yaw rate back to their equilibrium values. It is important to note that this controller response occurs even though the vehicle state trajectories have deviated significantly from the drift equilibrium at which the controller has been designed.

## 6.3. Interaction of yaw rate and sideslip dynamics

The effect of the disturbance at  $t = 6.5$  s on the vehicle's dynamics provides interesting insights into the role of yaw rate in the sideslip dynamics. Consider Figure 15, which presents yaw rate and sideslip measurements in the timeframe surrounding the disturbance. From these plots, it is evident that the yaw rate behaviour 'leads' the sideslip behaviour in the same fashion as observed for the stable state trajectories of the closed-loop system plotted in Figure 13. At the beginning of the disturbance, an abrupt drop in yaw rate precedes a more gradual decrease in sideslip angle magnitude, while a build-up in yaw rate just after  $t = 7.5$  s precedes a gradual return to the desired sideslip angle.

Figure 15.  $r$  and  $\beta$  during friction disturbance.Figure 16. Comparison of  $a_y$ ,  $rv_x$ , and  $v_y$  during friction disturbance.

This behaviour can be explained by analysing experimental measurements of the quantities that dictate  $\dot{v}_y$ . Because the vehicle velocities  $v_x$  and  $v_y$  are defined in a vehicle-fixed frame,  $\dot{v}_y$  is related to the vehicle's lateral acceleration  $a_y$ , yaw rate  $r$ , and longitudinal velocity  $v_x$  as follows:

$$\dot{v}_y = a_y - rv_x. \quad (17)$$

By equating Equation (17) with the expression for  $\dot{v}_y$  in Equation (2), it becomes clear that  $a_y$  represents the combined influence of the tyre force terms upon the lateral dynamics, as indicated in Equation (18):

$$a_y = \frac{F_{y,f} \cos \delta + F_{y,r}}{m}. \quad (18)$$

Thus, by comparing experimental measurements of  $a_y$  and  $rv_x$  (as calculated from independent measurements of  $r$  and  $v_x$ ), it is possible to gauge the relative influence of the tyre force and  $rv_x$  terms in the lateral velocity dynamics. The top plot in Figure 16 compares the product  $rv_x$  with measurements of  $a_y$  (a raw measurement of  $a_y$  and a filtered version from a third-order acausal filter with a 5 Hz cutoff frequency are shown). It is apparent from the measurements of  $a_y$  that the sum of the tyre lateral forces remains fairly constant. In contrast,  $rv_x$  exhibits significant variation over a range three times larger than variation in the filtered  $a_y$ . Thus, the changes in  $\dot{v}_y$  are dominated by changes in the  $rv_x$  term. Since  $v_x$  is essentially constant over the course of the disturbance, this analysis suggests that yaw rate can be used as an ‘input’ to the lateral velocity dynamics in future controller designs.

## 7. Conclusions and future work

This work has presented a relatively simple analytical framework for understanding the dynamics of drifting. An equilibrium analysis of a rudimentary bicycle model with nonlinear tyres and a ‘de-rated’ rear friction coefficient reveals the existence of equilibria embodying the primary characteristics of steady-state drifting, including a large sideslip angle, countersteer, and rear tyre saturation. By applying techniques of nonlinear system analysis to the operating regime surrounding these equilibria, it has been verified that the drift equilibria are saddle points, with unusual non-minimum phase characteristics. The success of an autonomous drifting controller designed using linearisation about one of these drift equilibria is, to the best knowledge of the authors, a novel experimental achievement. Moreover, it validates the utility of simple analysis techniques for predicting vehicle behaviour in this dangerous operating regime and designing control algorithms for maintaining stability within this regime.

Future work will be focused upon refinement of control strategies for autonomous drifting that better account for the drifting techniques of skilled drivers, as well as the characteristics of the drift equilibria. The non-minimum phase characteristic of the dynamics from steering input to sideslip angle around a drift equilibrium suggests that a simple state feedback steering controller design may be susceptible to robustness issues. Given that parameter (especially friction) variation is inevitable on gravel and dirt surfaces, destabilisation due to the right half plane zero in these dynamics is a potential problem. Therefore, a controller design that circumvents these dynamics may achieve better robustness characteristics. The observations in Section 6.3 suggest that a successive loop control structure in which steering is used to control yaw rate and yaw rate is used to control sideslip would be an effective design for this purpose.

Additionally, significant performance improvements may be possible through incorporation of coordinated longitudinal control that goes beyond the simple speed feedback used in this work. This is evident from the experimental measurements in [3] and [4], in which skilled drivers are coordinating steering and throttle inputs to sustain a drift. However, there is also a concrete rationale for exploring coordinated longitudinal control from the analysis of equilibria in this work. Since equilibrium front tyre lateral force is nearly saturated at drift equilibria, front steering has limited control authority when an increase in front tyre lateral force is necessary. This limits the steering controller’s ability to respond to a sudden reduction in yaw rate or sideslip angle due to a friction disturbance, which may account for the large deviations in yaw rate and sideslip angle observed in the experimental data during such a disturbance. Coordinated longitudinal control could effectively address this issue, especially in the successive loop control structure proposed previously; an increase in rear longitudinal force and the resulting reduction in rear tyre lateral force could be used to increase yaw rate instead of an increase in front tyre lateral force.

## Acknowledgements

The authors gratefully acknowledge Electronics Research Lab of Volkswagen of the USA and the Frank H. and Eva B. Buck Foundation for supporting this work.

## References

- [1] T. Gustaffsson, *Computing the ideal racing line using optimal control*, MSc thesis, Linköping University, 2008.
- [2] E. Velenis and P. Tsiotras, *Minimum time vs maximum exit velocity path optimization during cornering*, IEEE International Symposium on Industrial Electronics, Dubrovnik, Croatia, 2005.
- [3] M. Abdulrahim, *On the Dynamics of Automobile Drifting*, Proceedings of the SAE World Congress, Detroit, MI, USA, 2006.
- [4] J. Edelmann, M. Plochl, P. Lugner, W. Mack, and A. Falkner, *Investigations on the Powerslide of Automobiles*, Proceedings of the AVEC'08, Kobe, Japan, 2008.
- [5] E. Ono, S. Hosoe, and H.D. Tuan, *Bifurcation in vehicle dynamics and robust front wheel steering control*, IEEE Trans. Control Syst. Technol. 6 (1998), pp. 412–420.
- [6] D.-C. Liaw, H.-H. Chiang, and T.-T. Lee, *Elucidating vehicle lateral dynamics using a bifurcation analysis*, IEEE Trans. Intell. Transp. Syst. 8 (2007), pp. 195–207.
- [7] E. Fiala, *Seitenkräfte am rollenden Luftreifen*, ZVDI 96 (1954), pp. 973–979.
- [8] S. Laws, C. Gadda, S. Kohn, P. Yih, J.C. Gerdes, and J.C. Milroy, *Steer-by-wire Suspension and Steering Design for Controllability and Observability*, Proceedings of the IFAC World Congress, Prague, Czech Republic, 2005.
- [9] J. Ryu and J.C. Gerdes, *Integrating inertial sensors with GPS for vehicle dynamics control*, J. Dyn. Syst. Meas. Control 126(2) (2004), pp. 243–254.
- [10] E.J. Rossetter, J.P. Switkes, and J.C. Gerdes, *Experimental validation of the potential field lanekeeping system*, Int. J. Autom. Technol. 5 (2004), pp. 95–108.